

UCSF

UC San Francisco Previously Published Works

Title

Inhibition of MET Signaling with Ficlatusumab in Combination with Chemotherapy in Refractory AML: Clinical Outcomes and High-Dimensional Analysis.

Permalink

<https://escholarship.org/uc/item/3d81k1m0>

Journal

Blood cancer discovery, 2(5)

ISSN

2643-3230

Authors

Wang, Victoria E
Blaser, Bradley W
Patel, Ravi K
et al.

Publication Date

2021-09-01

DOI

10.1158/2643-3230.bcd-21-0055

Peer reviewed

Inhibition of MET Signaling with Ficlatusumab in Combination with Chemotherapy in Refractory AML: Clinical Outcomes and High-Dimensional Analysis



Victoria E. Wang^{1,2}, Bradley W. Blaser³, Ravi K. Patel⁴, Gregory K. Behbehani³, Arjun A. Rao⁴, Blythe Durbin-Johnson⁵, Tommy Jiang^{1,2}, Aaron C. Logan^{1,2}, Matthew Settles⁵, Gabriel N. Mannis¹, Rebecca Olin^{1,2}, Lloyd E. Damon^{1,2}, Thomas G. Martin^{1,2}, Peter H. Sayre^{1,2}, Karin M. Gaensler^{1,2}, Emma McMahon^{1,2}, Michael Flanders^{1,2}, Vivian Weinberg¹, Chun J. Ye¹, David P. Carbone³, Pamela N. Munster^{1,2}, Gabriela K. Fragiadakis^{4,6,7}, Frank McCormick², and Charalambos Andreadis^{1,2}



ABSTRACT

Acute myeloid leukemia (AML) patients refractory to induction therapy or relapsed within 1 year have poor outcomes. Autocrine production of hepatocyte growth factor by myeloid blasts drives leukemogenesis in preclinical models. A phase Ib trial evaluated ficlatuzumab, a first-in-class anti-HGF antibody, in combination with cytarabine in this high-risk population. Dose-limiting toxicities were not observed, and 20 mg/kg was established as the recommended phase II dose. The most frequent treatment-related adverse event was febrile neutropenia. Among 17 evaluable patients, the overall response rate was 53%, all complete remissions. Phospho-proteomic mass cytometry showed potent on-target suppression of p-MET after ficlatuzumab treatment and that attenuation of p-S6 was associated with clinical response. Multiplexed single-cell RNA sequencing using prospectively acquired patient specimens identified IFN response genes as adverse predictive factors. The ficlatuzumab and cytarabine combination is well tolerated, with favorable efficacy. High-dimensional analyses at single-cell resolution represent promising approaches for identifying biomarkers of response and mechanisms of resistance in prospective clinical studies.

SIGNIFICANCE: This study demonstrates a favorable safety profile and promising clinical activity of ficlatuzumab and cytarabine in high-risk AML, thus supporting further investigation of this combination in a randomized trial. It also shows the utility of a novel application using multiplexed single-cell analyses to detect on-target activity and identify biomarkers of response.

INTRODUCTION

Acute myeloid leukemia (AML) is a rapidly fatal disease characterized by uncontrolled proliferation of malignant cells in the blood and the bone marrow (1). Standard induction therapy for patients with good performance status consists of anthracycline and cytarabine combination, termed “7 + 3.” While some achieve a complete remission (CR) with this regimen, approximately 20% to 40% of patients fail to respond or relapse soon thereafter. The therapy with the greatest curative potential for patients with relapsed or refractory disease is an allogeneic hematopoietic cell transplant (HCT). Cytarabine-containing regimens remain the cornerstone of salvage chemotherapy prior to HCT, although no single regimen is considered standard (2, 3). Even with an intensive regimen, only 30% of patients achieve a CR with a median survival of

7.5 months (4). Therefore, an urgent need exists for novel therapies to improve patient outcomes in this setting.

Studies have demonstrated the importance of the MET/HGF pathway in mediating treatment resistance and tumorigenesis across many tumors, including AML (5–7). MET encodes a receptor tyrosine kinase (RTK), and its only natural ligand is HGF (8). HGF binding leads to receptor dimerization, intracellular tyrosine (Y1234 and 1235) phosphorylation, and activation of the RAS/MAPK and the PI3K/AKT pathways, which mediate cellular proliferation, invasion, and survival. Using a loss-of-function short hairpin RNA screen, Kentsis and colleagues demonstrated that autocrine secretion of HGF was important for AML leukemogenesis (7). Genetic depletion of HGF using antibodies or MET inhibitors suppressed the growth of AML cells with aberrant HGF expression. In addition, elevated HGF expression was observed in a broad panel of myeloid-monocytic cell lines (23/28; ref. 9). Finally, retrospective series have shown that high serum HGF correlates with more aggressive disease and shortened survival (10–13).

We hypothesized that HGF depletion using the first-in-class mAb ficlatuzumab in combination with high-dose cytarabine (HiDAC) would improve clinical outcomes in patients with relapsed/refractory AML through abrogation of the MET signaling pathway. To this end, an investigator-initiated phase Ib trial (NCT02109627) was conducted. Multiplex high-dimensional profiling using single-cell RNA sequencing (scRNA-seq) of over 114,000 prospectively collected peripheral blood mononuclear (PBMC) single cells from 12 patients, across five time points, paired with mass cytometry (CyTOF), assessed changes during treatment to identify potential biomarkers and mechanisms correlated with response and resistance (14–16). On-target action of ficlatuzumab downregulated p-MET. Phosphoprotein suppression downstream of MET was correlated with response

¹Department of Medicine, University of California, San Francisco, San Francisco, California. ²Helen Diller Comprehensive Cancer Center, University of California, San Francisco, San Francisco, California. ³The Ohio State University Comprehensive Cancer Center, Columbus, Ohio. ⁴CoLabs, University of California, San Francisco, San Francisco, California. ⁵Bioinformatics Core, Genome Center, University of California, Davis, Davis, California. ⁶Bakar ImmunoX Initiative, University of California, San Francisco, San Francisco, California. ⁷Department of Medicine, Division of Rheumatology, University of California, San Francisco, San Francisco, California.

V.E. Wang and B.W. Blaser contributed equally to this article.

Corresponding Author: Charalambos Andreadis, UCSF Helen Diller Comprehensive Cancer Center, 400 Parnassus Avenue, San Francisco, CA 94143. Phone: 415-353-2051; Fax: 415-353-2467; E-mail: charalambos.andreadis@ucsf.edu

Blood Cancer Discov 2021;2:434–49

doi: 10.1158/2643-3230.BCD-21-0055

©2021 American Association for Cancer Research

to the drug. Additional predictive transcription signatures were identified throughout the treatment course. Overall, this study highlights the prospective dynamic changes in AML in response to the novel agent ficlatuzumab at a high cellular and molecular resolution.

RESULTS

Ficlatuzumab and High-Dose Cytarabine Is Well Tolerated in Primary Induction-Refractory AML

Between January 2014 and October 2018, a total of 18 patients were consented and 17 enrolled in the trial. One patient was ineligible due to active fungal pneumonia. Full clinical characteristics are summarized in Table 1 and further delineated for each patient in Supplementary Table S1. The median age was 58 years (range 22–74), with four patients over the age of 65. Thirteen patients had *de novo* AML, three had secondary AML, and one had MDS, RAEB-2. A total of 41.2% of the patients (7/17) exhibited a complex karyotype, defined as three or more independent abnormalities, and 23.5% (4/17) harbored 5q deletion. Mutations in FLT3-ITD, TKD, NPM1, GATA2, MECOM, TP53, and ASXL1 were each observed in one patient (5.9%); RUNX1 in two patients (11.8%); and IDH2 in three patients (17.6%). By virtue of their cytogenetics or gene mutations, 88.2% (15/17) of patients received the 7 + 3 induction regimen initially and 70.6% (12/17) exhibited poor-risk disease at diagnosis as defined by the European LeukemiaNet (ELN) guidelines (17). All patients were primary induction refractory, with a baseline median white blood cell count of $7.04 \times 10^9/L$ (range 0.1–55.7) and 19% bone marrow blasts (range 4.5–95).

Three patients were enrolled in each dose-escalation cohort (Fig. 1A), and PBMCs, sera, and bone marrow biopsies were collected at prespecified time points (Fig. 1B). Sixty-five percent (11/17) of the patients completed all planned doses of ficlatuzumab induction. No delay in the drug administration was observed. Eleven doses (16%) of ficlatuzumab were missed in six patients who discontinued treatment due to progression of disease (three patients), sepsis (one patient), upper gastrointestinal bleeding (GIB; one patient) and starting consolidation at physician's discretion (one patient; Table 2; Supplementary Table S1). Three patients, all responders, received extra ficlatuzumab doses (seven total) during consolidation at the physician's discretion (Supplementary Table S1). No protocol-defined dose-limiting toxicities (DLT) were identified, and the 20 mg/kg dose of ficlatuzumab was chosen for the dose-expansion cohort. Supplementary Table S2 shows all treatment-emergent adverse events (AE). The most common toxicity and \geq grade 3 AE was febrile neutropenia (9/17; 53%; Table 2). Other common toxicities included sepsis (3/17; 17%), esophagitis and ulceration, GIB, and hypotension (2/17; 12% each). None of these were attributed specifically to ficlatuzumab except possibly for GIB. Serious AEs (SAE) occurred in two patients (12%; Supplementary Table S3). There was one death from complication of sepsis (grade 5), unrelated to the study drug. Another experienced grade 4 GIB after the first dose of ficlatuzumab at 20 mg/kg, which recurred after a second dose. Thus, further treatment with ficlatuzumab was discontinued. Because this isolated episode occurred during the dose-expansion phase, it is considered an

Table 1. Patient demographic and baseline characteristics

| Characteristic (n = 17) | N (%) |
|---|-----------------|
| Age, y | |
| ≥ 65 | 4 (23.5%) |
| < 65 | 13 (76.5%) |
| Median (range) | 58 (22–74) |
| Sex | |
| Male | 10 (58.8%) |
| Female | 7 (41.2%) |
| ECOG Performance Status | |
| ≤ 1 | 17 (100%) |
| Diagnosis | |
| <i>De novo</i> AML | 13 (76.5%) |
| Secondary ^a | 3 (17.6%) |
| MDS, RAEB-2 | 1 (5.9%) |
| Relapsed versus primary refractory | |
| Primary refractory | 17 (100%) |
| Risk category (ELN 2017) | |
| Favorable | 1 (5.9%) |
| Intermediate | 4 (23.5%) |
| Poor | 12 (70.6%) |
| Cytogenetics | |
| Complex karyotype | 7 (41.2%) |
| 5q deletion | 4 (23.5%) |
| Monosomal karyotype | 1 (5.9%) |
| Normal karyotype | 5 (29.4%) |
| Mutations | |
| FLT3-ITD | 1 (5.9%) |
| FLT3-TKD | 1 (5.9%) |
| IDH1 or 2 | 3 (17.6%) |
| NPM1 | 1 (5.9%) |
| GATA2 | 1 (5.9%) |
| MECOM | 1 (5.9%) |
| TP53 | 1 (5.9%) |
| RUNX1 | 2 (11.8%) |
| ASXL1 | 1 (5.9%) |
| Baseline white cell blood count ($\times 10^9/L$) | |
| ≥ 30 | 2 (11.8%) |
| ≥ 10 to < 30 | 1 (5.9%) |
| < 10 | 14 (82.3%) |
| Median (range) | 7.04 (0.1–55.7) |
| Baseline bone marrow blast count (%) | |
| ≥ 50 | 6 (35.3%) |
| ≥ 20 to < 50 | 2 (11.8%) |
| < 20 | 9 (52.9%) |
| Median (range) | 19 (4.5–95) |
| Prior therapies | |
| 7 + 3 ^b | 15 (88.2%) |
| Others ^c | 2 (11.8%) |

NOTE: Date of censoring: June 30, 2020.

Abbreviations: ECOG, Eastern Cooperative Oncology Group; ELN, European LeukemiaNet; MDS, RAEB-2, myelodysplastic syndrome, refractory anemia with excess blasts type 2.

^aIncludes AML with myelodysplasia-related changes ($n = 1$), therapy-related myeloid neoplasm ($n = 1$), and evolved from chronic myelomonocytic leukemia ($n = 1$).

^bIncludes two patients who subsequently received 5 + 2.

^cOne patient received ADE (cytarabine, daunorubicin, and etoposide) and the other azacitidine plus venetoclax and daunorubicin.

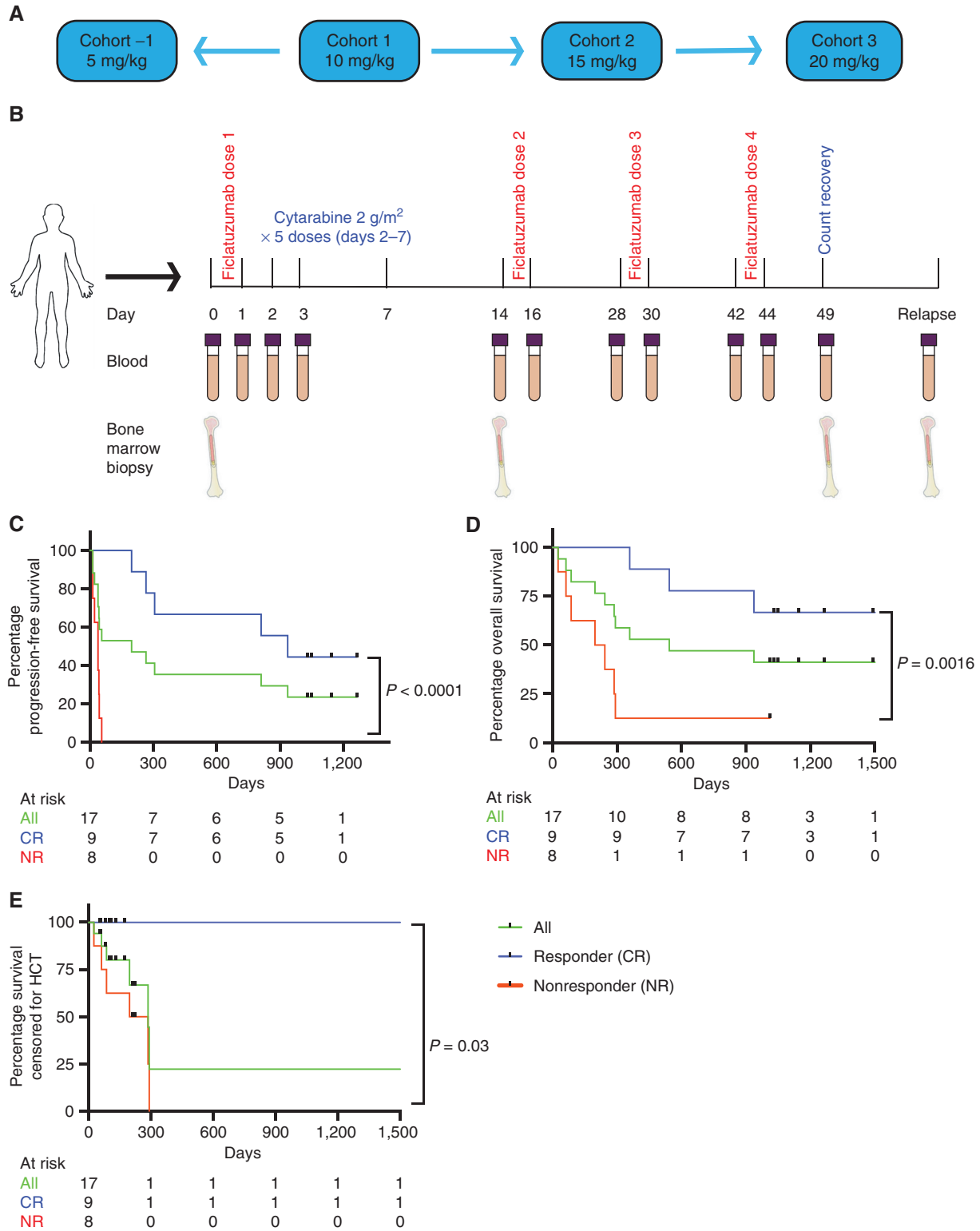


Figure 1. Trial schema and endpoints. **A**, Dose-escalation scheme utilizing the traditional 3 + 3 design. Ficlitzumab was started at the 10 mg/kg dose and escalated by increments of 5 mg/kg while keeping the dose of cytarabine fixed at 2,000 mg/m². **B**, Timeline for drug administration and biospecimen acquisition. Bone marrow biopsies were collected at baseline, on day 14, at count recovery, and at disease relapse. Blood collection occurred at baseline, on days 1 to 3, prior to and 24 hours after each subsequent doses of ficlitzumab at count recovery, and at relapse. **C**, Kaplan-Meier curves for progression-free survival. **D**, Kaplan-Meier curves for overall survival. **E**, Kaplan-Meier curves for overall survival censored at time of allogeneic stem cell transplant. *P* values indicate comparison between responders and nonresponders. All patients (green), responders (blue), and nonresponders (red).

Table 2. Grade ≥ 3 adverse events, mortality, and doses of drug administered

| Event (n = 17) | N (%) |
|---|----------|
| Febrile neutropenia | 9 (53%) |
| Sepsis | 3 (17%) |
| Esophagitis/ulcers | 2 (12%) |
| GIB | 2 (12%) |
| Hypotension | 2 (12%) |
| LFT elevation | 1 (6%) |
| Hypokalemia | 1 (6%) |
| Respiratory distress | 1 (6%) |
| Multi-organ failure | 1 (6%) |
| 30-Day mortality | 1 (6%) |
| 60-Day mortality | 1 (6%) |
| Total doses of ficlatuzumab administered ^a | 64 |
| Delayed doses ^b | 0 (0%) |
| Missed doses ^c | 11 (16%) |

NOTE: Date of censoring: June 30, 2020.

Abbreviation: LFT, liver function test.

^aTotal doses of ficlatuzumab included four doses during induction per patient and any dose given as consolidation at the treating physician's discretion.

^bDelayed doses only included induction (n = 68), since initiation of consolidation may be variable.

^cMissed doses only accounted for dose during induction, since not all patients received ficlatuzumab consolidation.

idiosyncratic reaction rather than a DLT. The 30- and 60-day mortality was 6% (1/17).

Overall response rate (ORR) based on bone marrow biopsy was 53% (9/17), all CRs (Supplementary Table S1). Sixteen patients had minimal residual disease (MRD) status assessed, and four of the nine responders were MRD negative (E5, 6, 9, and 14). Ten patients, eight responders and two nonresponders, proceeded to allogeneic HCT. Among these, six patients currently remain in remission. Full transplant characteristics are summarized in Supplementary Tables S4 and S5. Median time from start and the last dose of ficlatuzumab to transplant are 107 and 64 days, respectively (range 64–224 and 23–172). Fludarabine and busulfan was the most common conditioning regimen used, and 40% (4/10) of the patients also received rATG. One person received clofarabine and melphalan, one fludarabine/cyclophosphamide/low-dose total body irradiation using a haploidentical protocol, and another cyclophosphamide/etoposide/total marrow and lymphoid irradiation for active disease. Sixty percent (6/10) had matched unrelated donors, and 40% (4/10) had sibling donors. Fifty percent (5/10) of the donors were exact haplotype matches. One was a haploidentical sibling donor. Three patients received post-HCT azacitadine due to poor-risk disease. Another patient had early-relapse post-HCT that showed molecular evolution of new BCR–Abl and RUNX mutations, underwent reinduction with HiDAC, dasatinib, and sorafenib, and remained in remission with negative BCR–Abl PCR on maintenance ponatinib. At the time of censoring

on June 30, 2020, the median progression-free survival (PFS) and overall survival (OS) for all patients were 6.6 and 18.1 months, respectively, and 31.2 months and not yet reached for responders (Fig. 1C and D). When censored for allogeneic HCT, the OS was 9.5 months for all patients and not yet reached for responders (Fig. 1E).

Ficlatuzumab's On-Target Effect Potentially Suppresses the MET Axis

To assess the target engagement of ficlatuzumab in the serum, hHGF ELISA was performed using banked sera from the dose-escalation cohort (E1–9) at baseline and at predefined time points. When compared with normal controls, there was no discernible difference in baseline HGF levels and no difference between responders (n = 4) versus nonresponders (n = 5; Supplementary Fig. S1A and S1B). Samples were run in triplicate, and the results averaged (Supplementary Fig. S1C and S1D). Addition of ficlatuzumab did not affect detection of HGF over the range of HGF concentrations detected in human sera (Supplementary Fig. S1E and S1F).

Mass cytometry (CyTOF) was employed to more precisely quantitate the on-target action of ficlatuzumab. Antibodies were conjugated with isotopically pure heavy metals to identify surface markers and intracellular phosphoproteins on the single-cell level with minimal overlap in metal signals. The custom panel of 33 antibodies, including 11 phosphoproteins (Supplementary Table S6), characterized the major cellular subsets and the key intracellular signaling pathways downstream of MET (STAT, MAPK, and PI3K/AKT). The T-cell subgroups were identified using CD3⁺, CD4⁺, CD7⁺, or CD8⁺. Similarly, the B-cell population expressed CD19; natural killer (NK) cells were CD7⁺ and CD3⁺; and plasmacytoid dendritic cells (pDC) had CD123⁺ and HLA-DR⁺. CD34⁺ and CD33⁺ defined the early and late myeloid populations, respectively, because monocytes expressed CD33⁺ and HLA-DR⁺, and were CD19[−]. Early granulocytes were CD33⁺, CD16⁺, and HLA-DR[−] (Supplementary Fig. S2A).

In total, PBMCs from eight patients (E1, 3–5, 7, 9, 12, and 13) and an untreated healthy control were analyzed using CyTOF. Where the cell numbers were limited (E2, 6, 11, and 8), the samples were prioritized for scRNA-seq instead of CyTOF. Samples included baseline prior to treatment initiation (time zero), 24 hours (day 1), and 48 hours (day 2) after the first dose of ficlatuzumab but prior to the administration of cytarabine and 24 hours after the first dose of cytarabine (day 3; Fig. 1B). The day 1 and day 2 samples reflected the only time points during the study where the ficlatuzumab-specific consequences may be studied without the confounding effects from systemic cytarabine. Because ficlatuzumab is an HGF-directed antibody, its binding to HGF would inhibit phosphorylation and subsequent activation of the MET RTK. CyTOF analyses using two independent methods, uniform manifold approximation and projection (UMAP; ref. 18) and spanning-tree progression analysis of density-normalized events (SPADE; ref. 19), demonstrated statistically significant on-target attenuation of p-MET in ficlatuzumab-treated patients compared with control in both the CD34⁺ (P = 0.01 UMAP and 0.04 SPADE) and CD33⁺ (P = 0.02 UMAP and 0.014 SPADE) myeloid compartments (Fig. 2A–C). The change in T-MET was not statistically significant (Fig. 2D and E). Pervanadate stimulation,

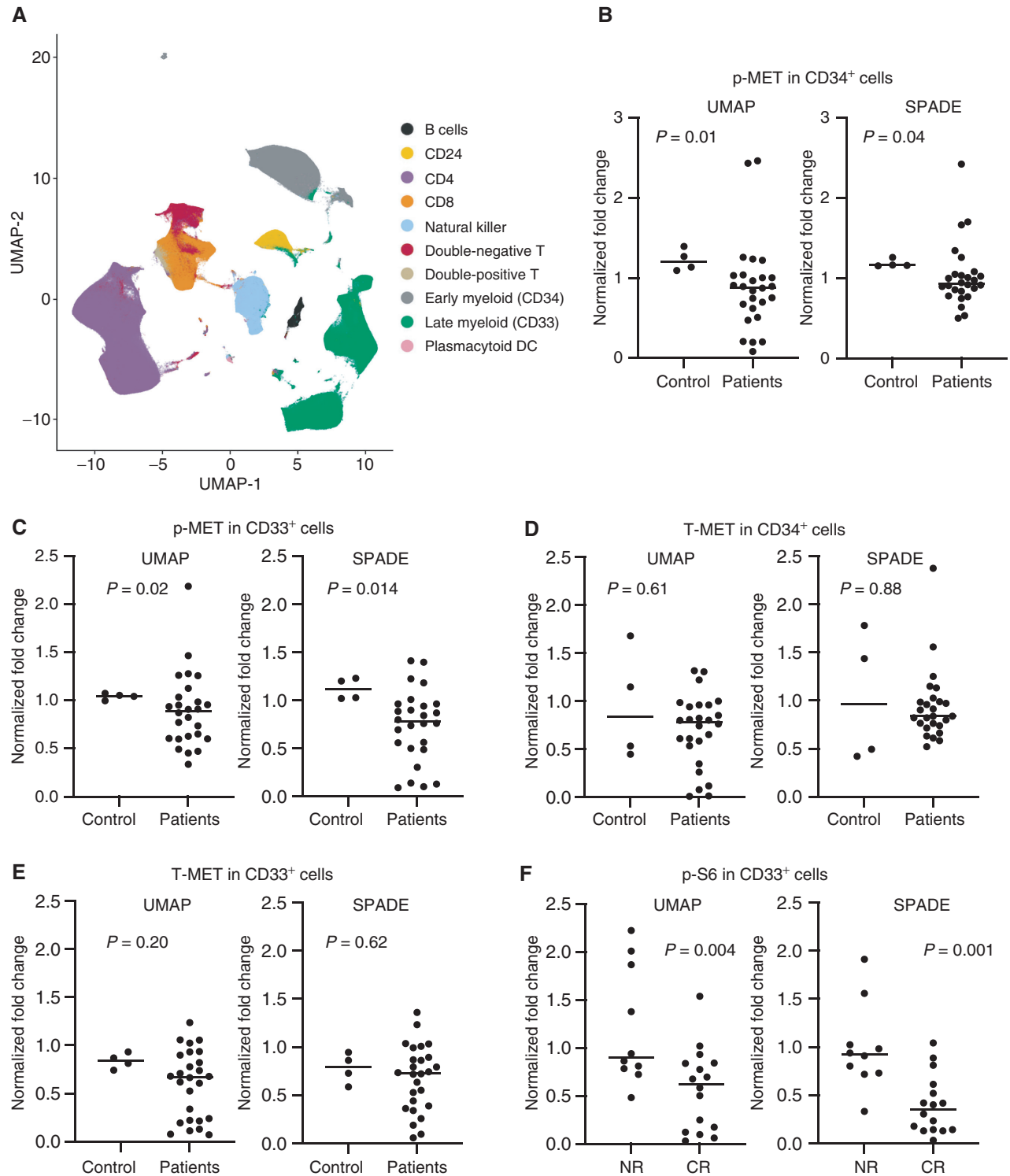


Figure 2. Ficlitzumab treatment exerts on-target effect through attenuation of p-MET. **A**, UMAP representation of mass cytometry data according to cellular identity after filtering for debris. **B**, p-MET expression in the CD34⁺ early myeloid compartment between all patients, independent of pervandate stimulation, versus untreated control as assessed by UMAP and SPADE. **C**, p-MET expression in the CD33⁺ myeloid compartment between all patients, independent of pervandate stimulation, versus untreated control as assessed by UMAP and SPADE. **D**, T-MET expression in the CD34⁺ early myeloid compartment between all patients versus untreated control. **E**, T-MET expression in the CD33⁺ myeloid compartment between all patients versus untreated control as assessed by UMAP and SPADE. **F**, Differential p-S6 expression between nonresponders (NR) and responders (CR) using both UMAP and SPADE. *P* values calculated using the Mann-Whitney test.

which blocks endogenous tyrosine phosphatases, augmented the p-MET signals in some treated samples but did not appear to alter the trajectory of their expression over time to any appreciable extent (20). The initial level of p-MET and p-S6 and their changes over time, in the presence and absence of pervanadate, are shown in Supplementary Fig. S2B–S2E. These observations were consistent with our original hypothesis, suggesting that the myeloid-derived cells demonstrated greater sensitivity toward inhibition of the HGF–MET axis.

Degree of Effector Pathway Attenuation Correlates with Response to Ficlatusumab

To explore potential predictive phospho-proteomic biomarkers, we classified patients by their clinical responses. Patients E1, 3, and 7 progressed on study, while the others achieved CR. All three patients in cohort 1 exhibited disease progression. Patient 5 in cohort 2 received 15 mg/kg of ficlatusumab, while the others received 20 mg/kg. Effector pathways examined in the CyTOF panel included MAPK, PI3K/ATK, JAK/STAT, NF- κ B, p-CREB, and p-PLC γ 2. Each sample was divided in half, and one was stimulated with pervanadate, while the other was not. The ratio in protein expression level at 24 and 48 hours post-ficlatusumab was normalized relative to the protein expression at time zero. Because protein expression trended similarly at 24 and 48 hours (Supplementary Fig. S2B–S2E) and the unstimulated versus stimulated samples showed concordant changes over time, clinical response was the only variable used for stratification during statistical analysis. Surprisingly, p-MET expression was not predictive of response in either the CD34⁺ ($P = 0.42$ UMAP and 0.2 SPADE) or CD33⁺ cells ($P = 0.24$ UMAP and 0.59 SPADE; Supplementary Figs. S3A and S3B and S4A and S4B). Only p-S6 was significant in the CD33⁺ population after Bonferroni adjustment ($P = 0.004$ by UMAP and 0.001 by SPADE, respectively; <0.005 ; Fig. 2F). None of the other downstream effector pathways reached statistical significance using both analyses after Bonferroni correction (Supplementary Figs. S2A and S2B and S3A and S3B). p-S6 has been implicated to be a direct target of TORC1, which functions downstream of both the PI3K/AKT and the MAPK pathways, the latter likely through a TORC-1 independent, p90 ribosomal S6 kinase (RSK)–dependent mechanism (21). Emergence of p-S6 suppression as a biomarker for predicting ficlatusumab response underscores p-S6 as a point of convergence for key signaling axes downstream of MET, that is, PI3K and MAPK, and supports a linear relationship that attenuation of p-MET leads to repression of target proteins necessary for cellular growth and survival (22). These results suggest that the leukemic blasts may exhibit enhanced dependency on HGF–MET inhibition relative to other cell lineages.

Application of a Multiplexing scRNA-seq Platform to Identify Major Immune Subsets in PBMCs

To assess transcriptional biomarkers predictive of response, scRNA-seq was employed as a complementary high-dimensional analysis in addition to CyTOF. We used freemuxlet, a novel extension of the demuxlet algorithm that allows for multiplexing of distinct samples from unrelated individuals by using single-nucleotide polymorphisms (SNP; refs. 23–25). Freemuxlet identifies expressed SNPs in raw scRNA-seq data

and uses a Bayesian clustering algorithm to form N read groups on the basis of this genetic variance, where N is equal to the number of genetically unique samples in the pool.

Fifty-seven samples collected from 11 distinct AML patients (E1–7, E9, E11–13), at up to five time points each, were distributed among five distinct pools using a modified Latin Square design (Supplementary Fig. S5A). Each pool contained samples from genetically unrelated individuals at different time points to allow for demultiplexing using SNP variants and to minimize batch effects. Samples from the healthy control were added to each pool to ensure uniformity of cell capture and sequencing. Patient samples were genotyped using the Infinium OmniExpressExome-8 v1.6 Bead-Chip (Illumina), identifying thousands of unique variants per patients. Duplicate capture reactions using the 10x Chromium 3' capture technology were performed for each sample pool targeting 25,000 to 30,000 cells recovered. The number of cells captured in each reaction replicate demonstrated high concordance (Supplementary Fig. S5B). A total of 175,667 cells were captured over 10 reactions; 373 (0.2%) could not be assigned a genotype by freemuxlet and were deemed ambiguous, and 60,787 (34.6%) cells were identified as doublets using genetic variant data, a number expected with our initial loading conditions. Additional filtering was performed to remove low-quality cells based on percentage of reads mapped to mitochondrial genes and number of recovered genes. Demultiplexing was completed by matching single-nucleotide variants (SNV) in freemuxlet genetic clusters to known patient SNVs. Each freemuxlet-predicted cluster was matched to a unique patient cluster (Supplementary Fig. S5C).

Global gene expression was visualized in the scRNA-seq dataset using the UMAP method of dimensionality reduction in Monocle 3 (refs. 18, 26; Supplementary Fig. S6A and S6B). To reduce interpatient heterogeneity and to facilitate clustering, the mutual nearest neighbor alignment approach package Batchelor was utilized to account for batch preparation among individual samples (27). Unbiased cell clusters were defined using the partitioning method (Fig. 3A and B) with projection onto the unaligned dataset in Supplementary Fig. S6B (20). Initial cluster assignments were made by inspection of the top lineage-specific markers ($n = 50$) from each cluster (Fig. 3C; Supplementary Table S7). Broadly speaking, the myeloid lineage is divided into three clusters: a large population of cells strongly expressing markers of myeloid maturation including CD33⁺, CD14⁺, S100A9, and lysozyme (*LYZ*), termed “late”; a hematopoietic stem cell (HSC)–like population characterized by CD34⁺, GATA2, and the leukemia stem cell marker CD99, called “early”; and a smaller population with distinct transcriptomic signature and high expression encoding the AML marker HLA-DRB1, collectively termed “HLA-DR⁺” (28). T, B, plasma, and erythrocytic cell clusters were identified using canonical markers (Fig. 3C and D). A small cluster of dividing cells with strong expression of Ki-67 and tubulin was also observed. To confirm these supervised cluster assignments, automated cell-type analysis was performed by mapping to a highly annotated PBMC reference with Seurat v4 (Supplementary Fig. S6C; ref. 29). Supervised labeling of the malignant cell types matched well to the normal cell-type identifiers provided by Seurat: The late cluster corresponded to Seurat’s CD14 and CD16 monocytic clusters,

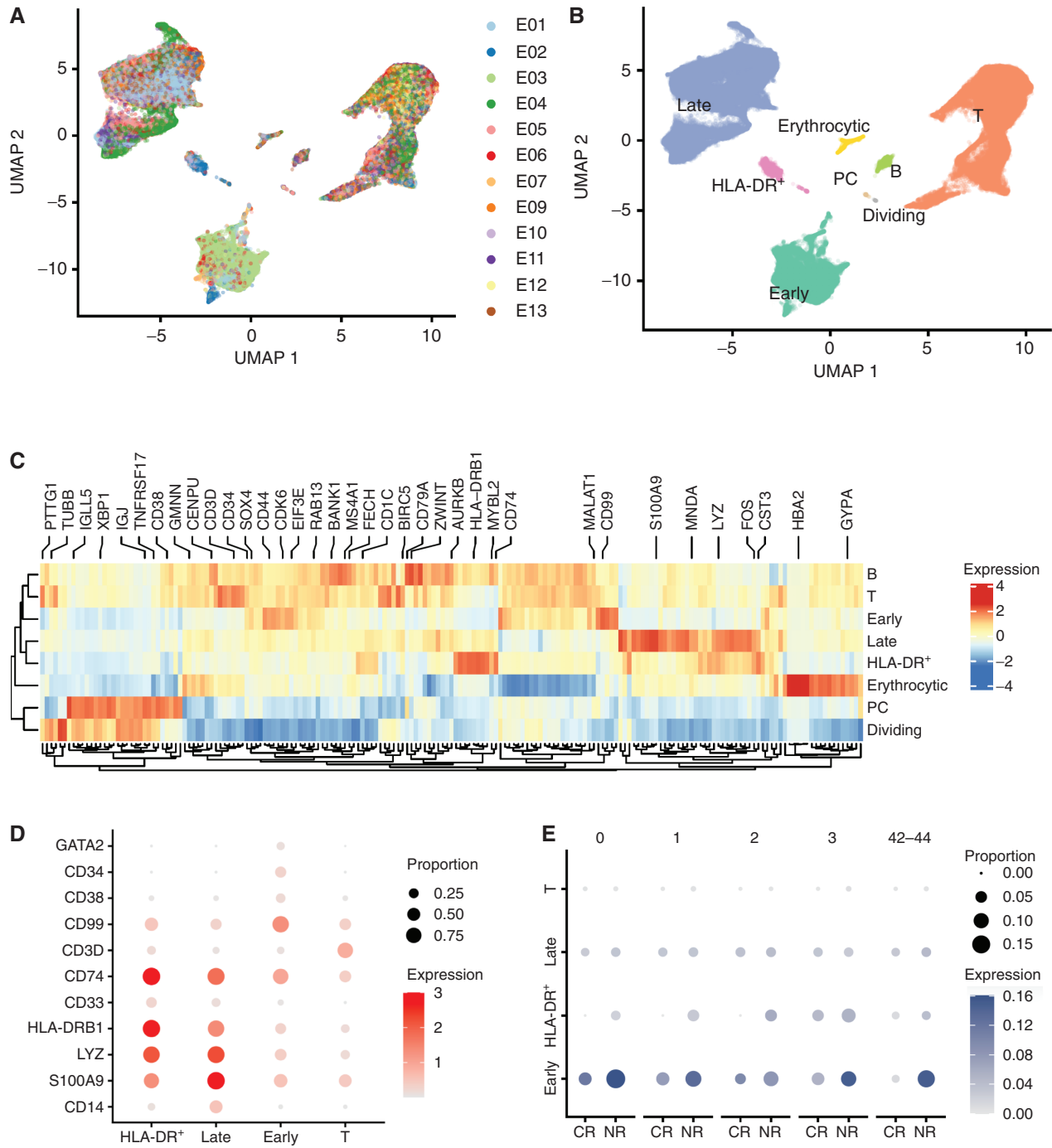


Figure 3. Cell-type identification and HGF expression using freemuxlet. **A**, Batch-corrected UMAP representation of all cells according to patient identity after filtering for doublets and low-quality cells. **B**, Batch-corrected UMAP partitioned using top expressed markers according to Jensen-Shannon divergence. PC, plasma cells. **C**, Heatmap of top expressed genes by cluster. **D**, Dot plot denoting major immune subsets versus lineage-specific markers. Size of the circles indicates proportion of cells expressing the particular marker. Color denotes mean expression in log scale. **E**, Dot plot quantifying temporal HGF expression across cell type and stratified by response and time. Circle size indicates proportion of cells expressing HGF. Color denotes mean HGF expression in log scale.

while the early cluster corresponded to Seurat's hematopoietic stem/progenitor cell cluster, and the HLA-DR⁺ group corresponded to Seurat's cDC1, cDC2, and AXL⁺ DC clusters.

To harmonize scRNA-seq and CyTOF expression data, equivalent cell populations in available samples were defined on the basis of CD33 and CD34 in CyTOF and observation of reads mapping to corresponding CD33 or CD34 in scRNA-seq data. For B and T cells, populations were defined on the basis of CD19 and CD20 for B cells and CD3 and CD7 for T cells in CyTOF, and assignment to the respective B- and T-cell partition in the scRNA-seq data. All CyTOF markers without 1:1 correspondence to scRNA-seq markers, such as phosphoproteins or specific protein isoforms such as CD45RA, were excluded. We compared the fractional contribution of each major cell type in samples where both CyTOF and scRNA-seq data were available. Log transformation was applied to improve linearity. Linear regression demonstrated a coefficient of determination (R^2) of 0.79 and $P < 2.2 \times 10^{-16}$ (Supplementary Fig. S6D). Furthermore, a correlation matrix was generated from the mean expression values for all remaining CyTOF/scRNA-seq marker pairs within each defined cell cluster (Supplementary Fig. S6E). The high degree of correlation between CyTOF and scRNA-seq markers and the cellular proportions identified using these two methods support our cell-type identification strategy and overall data quality.

Elevated HGF Expression Predicts a Lack of Response to Ficlatusumab

We hypothesized that induction of HGF could be a mechanism of resistance to ficlatusumab. Therefore, HGF expression would correlate with lack of clinical response to the study drug. To investigate the temporal dynamics of HGF expression, its expression in the malignant cell populations of all study patients, excluding the normal control, is shown in Fig. 3E and Supplementary Fig. S7A, with T cells included as a negative internal control. Smaller populations (B and dividing cells) have been omitted, since the population averages can be skewed by small samples. Regression analysis was performed using a generalized linear model with the negative binomial distribution to predict the expression of HGF. HGF expression was stratified by treatment day and clinical response. Response and partition assignment were included as predictors. Independent of partitioning, nonresponse to ficlatusumab was a statistically significant predictor of higher HGF expression on days 0, 1, and 42 to 44 relative to responders (day 0, $P = 0.0008$; day 1, $P = 0.016$; day 2, $P = 0.17$; day 3, $P = 0.26$; days 42–44, $P = 8.3 \times 10^{-7}$; Fig. 3E). HGF expression was restricted mainly to the early HSC-like, HLA-DR⁺, and late leukemia cell clusters, with low expression in nonmyeloid cells and in the normal control (Fig. 3E; Supplementary Fig. S7A). Together, these data support that HGF acts as a prosurvival factor stimulating the growth of myeloid blasts and that persistence of high HGF expression appears to be a mechanism of *de novo* resistance to ficlatusumab.

Recently, Edwards and colleagues reported that subpopulations of stromal support cells within the hematopoietic niche express CSF1R and that CSF1 stimulation results in HGF secretion, which activates cMET on the AML blasts, promoting their growth (30). We investigated the cellular expression pattern of CSF1R and demonstrated that it was

restricted primarily to the HLA-DR⁺ and the late leukemia clusters, with relatively low levels on B and T cells as well and the early cluster where HGF was highest (Supplementary Fig. S7B). Furthermore, HGF and CSF1R exhibited discordant expression patterns with respect to treatment day and clinical response. Whereas HGF expression was strongly induced in the nonresponders throughout the treatment course, especially at days 42 to 44, CSF1R expression was higher in nonresponders only on day 0 and day 1 and was lower in nonresponders compared with responders on days 2, 3, and 42 to 44, independent of partition assignment ($P = 0.02$, 0.001, and 0.03, respectively; Supplementary Fig. S7A–S7C).

We hypothesized that ficlatusumab inhibition of the HGF–c-Met pathway will lead to concomitant downregulation of HGF transcriptional targets. To test this, we interrogated the expression pattern of HGF target genes, identified through public databases (GSE12197), within our scRNA-seq data (31). Consistent with published reports, HGF blockade resulted in repression of its effectors and lower expression in the responders compared with nonresponders (Supplementary Fig. S7D). Of note, the MET expression could not be assessed due to its low level of expression in all lineages.

Gene Module Analysis Identifies Biomarkers of Response to Ficlatusumab

Gene module analysis was used to identify coregulated genes that define functionally relevant cellular states and to extrapolate a transcriptomic signature of response to ficlatusumab across this heterogeneous cellular population (32). Twenty gene modules were identified, with each module containing 35 to 4,817 genes (Supplementary Table S8). The aggregate expression for each module was calculated in cells from the early, late, and HLA-DR⁺ clusters and used to perform unsupervised, hierarchical clustering according to treatment day and response to therapy (Fig. 4A). Cells from the nonresponders partitioned separately from the responders and the controls. At count recovery (days 42–44), the responders clustered most closely with the normal controls (Fig. 4A). Four gene modules (3, 18, 1, and 7) accounted for this classification. While modules 3 and 18 were upregulated in nonresponders compared to responders throughout the treatment course, module 1 was strongly increased in responders. Module 7 exhibited the highest expression in nonresponders at days 0 and 42 to 44 and is the most closely associated with nonresponse to study therapy.

Gene Ontology (GO) term enrichment analysis using GOrilla and REVIGO was employed to identify biological pathways enriched in each of these modules and to collapse lists of GO terms based on semantic similarity, respectively (33, 34). Both modules 3 and 18, overexpressed in nonresponders, were highly enriched in genes for protein translation (Fig. 4B–E). Module 3 also contained additional genes related to cell–cell adhesion and signaling. Notably, nonresponders exhibited higher expression of p-S6 protein by CyTOF, which has been shown to correlate with and modulate protein translation (35, 36). Module 1, increased in responders, contained genes related to myeloid and leukocyte activation (Fig. 4F and G). Module 7, also overexpressed in nonresponders, was strongly enriched for type I IFN and viral

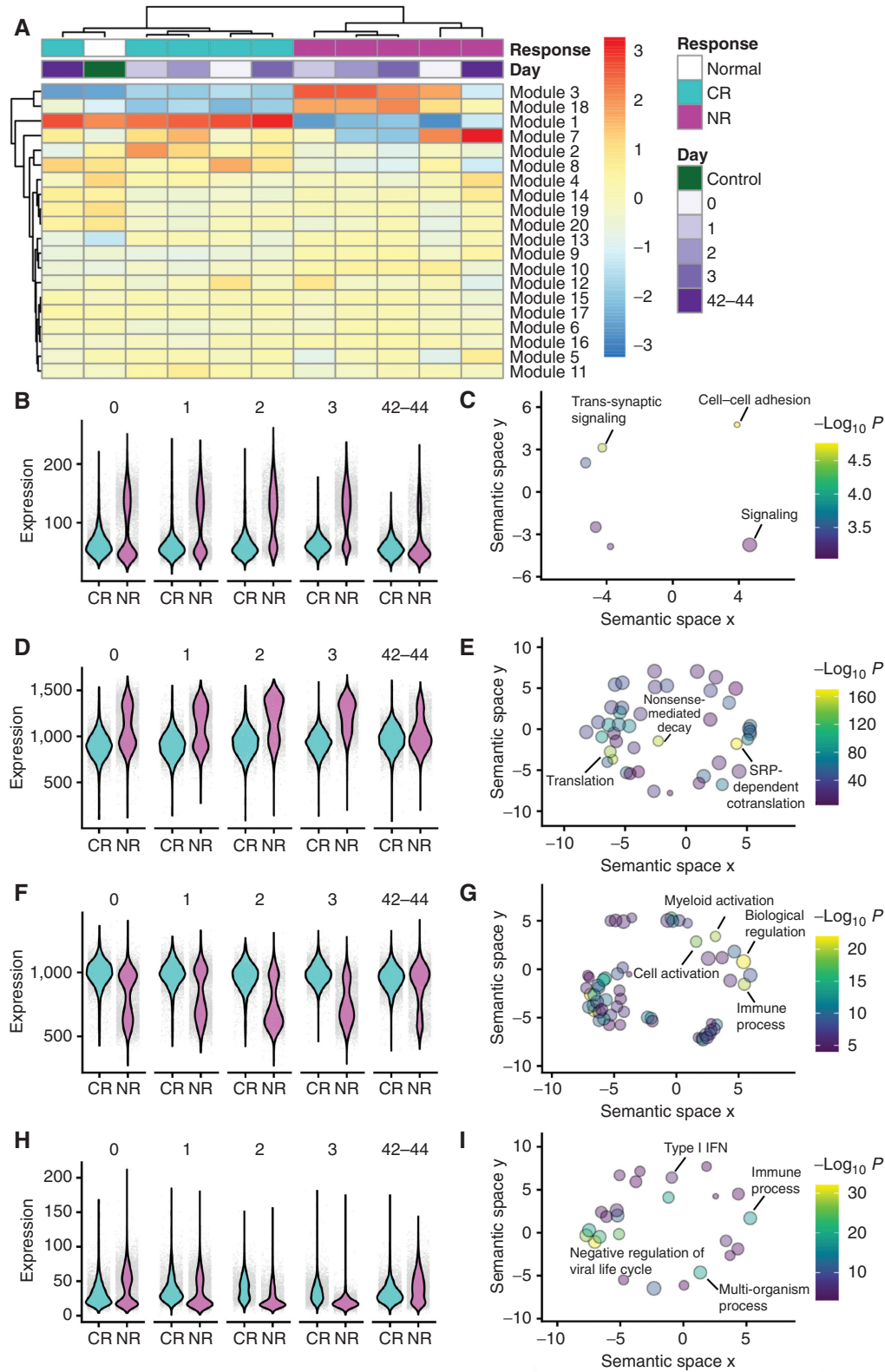


Figure 4. Gene module analysis identifies transcriptional signature as biomarkers of ficlatuzumab resistance. **A**, Unsupervised clustering of gene modules within the myelomonocytic lineage according to treatment day and clinical responses. **B**, Aggregated counts for module 3 genes in responders (CR) and nonresponders (NR) for each treatment time point. **C**, GO terms enriched in module 3. **D**, Aggregated counts for module 18 genes in CR and NR for each treatment time point. **E**, GO terms enriched in module 18. **F**, Aggregated counts for module 1 genes in CR and NR for each treatment time point. **G**, GO terms enriched in module 1. **H**, Aggregated counts for module 7 genes in CR and NR for each treatment time point. **I**, GO terms enriched in module 7.

response pathways, with a P value threshold of less than 10^{-11} (Fig. 4H and I). The type I IFN pathway has been associated with induction of proinflammatory cytokines such as IL6 to promote myelopoiesis and treatment resistance (37–39).

DISCUSSION

We conducted a phase Ib clinical trial of the novel HGF antibody ficlatuzumab targeting the MET axis combined with HiDAC in patients with induction-refractory AML. The dose-escalation portion of the study suggested that this combination was safe, and no DLTs were observed. The dose of 20 mg/kg of ficlatuzumab was chosen for the dose-expansion phase. The CR rate of 53% and median OS of 18.1 months observed in this study are promising for this high-risk population and quite favorable when compared with the CR rate of 30% and median OS of 7.5 months in the vosaroxin and HiDAC arm observed in the phase III VALOR trial using similar eligibility criteria (4). All patients who achieved a CR proceeded to allogeneic HCT except for one. None of these patients experienced any unexpected toxicities following allogeneic HCT.

An extensive series of correlative studies were conducted to further dissect the mechanism of ficlatuzumab action. Serum HGF levels did not reveal any significant differences following HGF blockade, likely due in part to the fact that the HGF capture antibody could not differentiate between free versus the ficlatuzumab-bound HGF. Thus, ELISA may overestimate the amount of circulating, functional HGF available.

To our knowledge, this represents the largest cohort of prospectively acquired, longitudinally analyzed single-cell dataset of patients with AML to date. Complementary high-dimensional profiling platforms were used—CyTOF and scRNA-seq—to investigate the proteomic and transcriptional alterations of PBMCs throughout the treatment course. Compared with serum levels, CyTOF offered superior resolution of on-target inhibition of the HGF receptor MET. HGF binding results in MET phosphorylation at multiple tyrosine residues, including Tyr1234/1235 assayed in CyTOF that are critical for kinase activation (22). This inhibition appeared to be dose dependent and specific within the myeloid lineage, because opposite effects were observed in T cells. Effector suppression downstream of MET, notably converging on p-S6, was strongly predictive of response to ficlatuzumab. These results suggest that the AML blasts may harbor a unique dependency on pharmacologic inhibition of MAPK and PIK3/AKT/TORC1 pathways because p-S6 integrates the output from both axes (21).

CytoF and scRNA-seq provide distinct advantages. Whereas both use unsupervised clustering to identify distinct cellular populations, scRNA-seq has the benefit of being entirely unbiased, whereas CyTOF utilizes preselected markers based on *a priori* knowledge. Multiplexing at the single-cell level allows for high throughput and significant conservation of time and cost, thus enabling identification of biomarkers and resistance pathways at deeper molecular resolution compared with prior studies. The analysis tool freemuxlet clusters cells based on similarity of a list of predefined SNP loci, derived from the 1000 Genomes reference panel, without knowledge of the precise patient SNPs

a priori. Each genetically defined freemuxlet cluster is then aligned to the patient genotype with the best match. Compared with demuxlet, freemuxlet improved the identification of the ambiguous cells by over 99%, reducing this group to less than 0.1% of the total cells captured, while the doublet rate remained similar, 34%. On the basis of this comparison, demuxlet may have limitations with regard to tumor cells due to the relative insensitivity of SNP profiling using chips. Because only a small fraction of these genomic SNP locations overlap with RNA-seq reads, the errors in genotypes from chips would severely impact the single-cell assignment to samples. On the other hand, freemuxlet uses a fixed set of genomic SNP locations that are known to vary among healthy individuals from the 1000 Genomes Project, and therefore focuses on the most reliable genomic locations for identifying the effective genotype of single cells. The 34% doublet rate derived from freemuxlet was consistent with published reports, based on our initial loading conditions of 40,000 to 50,000 cells per well, targeting a capture rate of ~60% (25,000–30,000; refs. 23, 40). The doublet rate was in fact lower than some studies, which reported an additional 15% to 20% error in cell count and multiple cell encapsulation 16% higher than predicted, possibly due to subsampling error or cell–cell interactions (40).

To harmonize the protein expression information from CyTOF with the scRNA-seq data, correlation matrix was generated from the mean expression values for the CyTOF/scRNA-seq marker pairs as well as the cell cluster proportions derived from each platform. Mean expression values showed an overall high degree of correlation between CyTOF and scRNA-seq markers with the exception of IL7R, which is a heterodimer, and CD38 and CD4, which are well-known to have poor RNA:protein correlation due to their tight transcriptional regulation and large dynamic range for protein expression (41, 42). The correlation between gene and protein expression in this study has exceeded prior reports, which estimated a Pearson correlation coefficient between 0.4 and 0.6 (43, 44). Similarly, cellular subset fractions demonstrated high concordance between scRNA-seq and CyTOF, further substantiating the overall data quality and our cell identification algorithm.

The discrepancies in transcript and protein expression underscore the need for new advances that allow for parallel measurement of transcript and protein phenotype at single-cell resolution using oligonucleotide-labeled antibodies such as cellular indexing of transcriptomes and epitopes by sequencing (CITE-seq) or RNA expression and protein sequencing (REAP-seq; refs. 45, 46). Inability for these methods to detect intracellular proteins and lack of well-characterized oligonucleotide-labeled antibodies for a wide array of proteins still limit their wide adoption as an immunophenotyping tool compared with mass cytometry. Through integration of our RNA and protein data, we identified that nonresponders exhibit higher expression of the p-S6 protein as well as higher transcript level of genes involved in protein translation compared with the responders. The concordant expression pattern of p-S6 and its target genes supports on-target suppression of the c-Met axis by ficlatuzumab on attenuating the c-Met axis and nominates p-S6 as a bona fide biomarker of clinical response.

Not surprisingly, the majority of the clusters did not exhibit salient transcriptional differences between responders and nonresponders except for the early, late, and HLA-DR⁺ populations. Several key observations emerged from this comparison. First, elevated HGF levels upon count recovery were correlated with lack of clinical response. Thus, persistent HGF expression may account for *de novo* resistance to HGF inhibitors. The mechanism underlying transcriptional activation of HGF, whether it is attributed to differential chromatin accessibility, autocrine stimulation, or paracrine stimulation of HGF, will be investigated in future studies. It is also interesting to note that the nonresponders exhibiting the highest HGF expression and most refractory to therapy exhibited a stem cell phenotype, a population that is traditionally more treatment resistant. Second, gene module analysis of responders demonstrated that gene expression in the early, late, and HLA-DR⁺ converged toward normal by count recovery but remained divergent in nonresponders. Finally, unsupervised clustering revealed differential regulation of the interferon inflammatory and translational initiation gene signatures between responders and nonresponders. Enrichment of the translational initiation signature in nonresponders strongly supports p-S6 as a biomarker of response, because p-S6 is a well-documented regulator of protein translation.

Complementary to our model, other studies substantiated the central role of HGF in driving AML tumorigenesis through paracrine activation of CSF1R in the stromal support cells (30). However, expression of HGF and CSF1R shared minimal overlap in our scRNA-seq dataset, which is not surprising because of the low numbers of macrophage-derived support cells circulating within the PBMCs. Future work will utilize banked bone marrow samples, combined with spatial profiling, to interrogate the interaction between HGF and CSF1R within the hematopoietic niche and test whether dual HGF and CSF1R blockade will lead to enhanced clinical responses.

Under physiologic condition, type I IFNs induce an antiproliferative state that defends against intracellular pathogens (47). IFN α also induces the secretion of proinflammatory cytokines, such as IL6, which activates myelopoiesis in response to infection and inflammation (39, 48). Blast cells are able to subvert this pathway to sustain malignant proliferation (37, 38). These data are consistent with findings in gene module 7, which is markedly elevated in nonresponders at baseline and at count recovery and enriched in IL6 and IFN response gene.

The proteomic and transcriptomic signatures from this study reveal hypothesis-generating insights into new biomarkers of response and future combination treatments for AML. The novel genetic multiplexing strategy based on naturally occurring SNP variations used in this study achieved high throughput in a cost-effective manner. Given the promising efficacy of this HGF-MET-directed combination, a multi-institutional, randomized phase II study is being contemplated, with high-dimensional correlative endpoints to validate the clinical activity observed as well as the biomarkers that emerged from this study. Longitudinal, single-cell profiling at higher sequencing depth of larger and more diverse cohorts while integrating the anatomic context of the tumor and its microenvironment using platforms such

as the multiparameter ion beam imager (MIBI) or digital spatial profiling (DSP) will (i) improve the molecular definition to subphenotype AML, (ii) enhance the resolution for annotating disease associations, and (iii) determine how the HGF-MET pathway modulates tumor stroma and leukemic blast interactions (49, 50). These analyses will provide a window into the natural history of AML that is challenging to achieve using bulk patient samples and serve as a proof-of-concept template for future translational studies to understand the mechanistic underpinnings of therapeutic response and resistance.

METHODS

Patients

Eligible patients were at least 18 years of age with histologically confirmed refractory AML or relapsed within 12 months of first CR/CR with incomplete hematologic recovery (CRi). Patients with refractory AML had either a hypercellular marrow with greater than 20% cellularity and 10% blasts at least 14 days after day 1 of induction or persistent disease documented by bone marrow biopsy at least 28 days after day 1 of induction. Participants could not have received more than two cycles of AML-directed therapy; one of them had to be an anthracycline and cytarabine combination. All patients had a documented ejection fraction greater than 40% and adequate organ function. Hypomethylating agents and cytoreduction therapy with plasmapheresis or hydroxyurea prior to study entry were acceptable. Patients were excluded for acute promyelocytic leukemia, previous cytarabine-containing regimen in excess of 2,000 mg/m²/day, grade 4 toxicity to cytarabine, prior anti-MET- or anti-VEGF-directed therapy, pregnancy, uncontrolled infection, HIV, hepatitis B, hepatitis C, or an active second malignancy. A complete list of inclusion and exclusion criteria is provided in the protocol (Supplementary Data).

Study Design and Objectives

In this investigator-initiated phase Ib study using the standard 3 + 3 design, patients received four doses of intravenous ficlatuzumab every 14 days (days 0, 14, 28, and 42) in combination with cytarabine. Ficlatuzumab dose started at 10 mg/kg in cohort 1, escalated to 15 mg/kg in cohort 2, and 20 mg/kg in cohort 3. This dosing was based on previous phase II studies conducted by AVEO. Fixed-dose cytarabine was administered daily at 2,000 mg/m² starting 48 hours after the first dose of ficlatuzumab for 5 days (days 2–7) for all dose levels. The study was approved by the Institutional Review Board of the University of California, San Francisco (UCSF; San Francisco, CA), and was conducted in accordance to the Declaration of Helsinki and Good Clinical Practices. Safety was monitored every 6 months by the UCSF Data Safety and Monitoring Committee. Written informed consent was obtained from all participants.

The primary objective of the study was to define the safety and the MTD of the ficlatuzumab and cytarabine combination. The secondary objectives included determining the rate of overall and complete remission and PFS. Exploratory objectives included assessing OS and biomarker changes throughout the treatment course.

Assessments

Patient who received per-protocol treatment were evaluated for pathologic response based on pretreatment and posttreatment bone marrow biopsies. The bone marrow specimens were evaluated by a hematopathologist using the Revised Recommendations of the International Working Group (51). Next-generation sequencing was performed using the ARUP Myeloid Malignancies Mutation panel and MRD testing using the commercial University of Washington multiparameter flow cytometry assay.

DLT was defined as (i) any drug-related grade 3 or higher nonhematologic toxicity despite optimal supportive care with the exception of rash, alopecia, fatigue, liver, ocular, central nervous system, or gastrointestinal toxicity expected from HiDAC or any disseminated intravascular coagulation, tumor lysis, fever, febrile neutropenia, infection, or sepsis expected with AML therapy; (ii) any toxicity resulting in ficlatuzumab dose reduction during therapy or an interruption of treatment for >2 weeks beyond the next scheduled ficlatuzumab dose; and (iii) delayed count recovery in the absence of residual disease as defined by failure to recover to absolute neutrophil count $\geq 1,000/\text{mcL}$ and/or transfusion-unsupported platelets $\geq 50,000/\text{mcL}$ by day 49 from the start of induction during the dose-escalation phase. PFS was evaluated from the time of study entry to evidence of disease recurrence, attrition from the study, change in treatment, or death with censoring at loss to follow-up. OS was measured from time of enrollment to death from any cause with censoring at loss to follow-up. AEs and laboratory values were graded according to the NCI Common Terminology Criteria for Adverse Events, v4.0 (52).

Mass Cytometry (Phospho-CyTOF) and Data Analyses

CyTOF was performed by the Human Immune Monitoring Center at Stanford University. Antibodies are listed in Supplementary Table S5. For antibody conjugation, 100 μg of carrier-free antibody was coupled to metal-labeled X8 polymer according to the manufacturer's instruction (Maxpar X8 Labeling Kit, Fluidigm). In brief, the lanthanide isotopic cations were chelated to Maxpar X8 polymers in L-buffer while the antibody was partially reduced in R-buffer and 4 mmol/L Tris (2-carboxyethyl)phosphine hydrochloride, pH 7.0 (Millipore Sigma). The lanthanide-loaded polymer was conjugated with the antibody in C-buffer, washed, and quantitated using the NanoDrop at 280 nm against a W-buffer blank (53). Gd157 was procured from Trace Sciences International and conjugated using the Maxpar X8 Kit. For staining, frozen PBMCs were thawed, transferred to RPMI with 10% FCS and benzonase (1:10,000 at 25 U/mL final concentration), washed, and filtered through a 70- μm cell strainer to ensure single-cell suspension. Normal PBMCs were included as controls. Each sample was aliquoted in duplicate of 10^6 cells in 200 μL of RPMI and placed in a 37°C incubator for 1 hour. Half of the samples were stimulated with pervanadate for 15 minutes at 37°C (Calbiochem, 125 $\mu\text{mol/L}$ final concentration in 1 mL of 0.53 mmol/L H_2O_2); 130 μL of 16% paraformaldehyde (EMS #15710-S) was added to each sample and incubated for an additional 10 minutes at room temperature. The cells were washed twice with 1 mL CyFACS buffer (Rockland, 1 \times PBS + 0.1% BSA, 2 mmol/L EDTA, and 0.05% sodium azide in MilliQ water). Subsequently, the samples were barcoded in batches of 10 using a unique combination of palladium antibodies according to manufacturer's protocol (Cell-ID20-Plex-Pd Bar Coding Kit, Fluidigm). A pretitrated mix of metal-conjugated surface antibodies was added to the combined samples in 180 μL and incubated for 30 minutes at room temperature. After washing, 1 mL of cold methanol was used to permeabilize the cells, and the samples were stored at -80°C overnight. For intracellular staining, the cells were thawed, stained first with the biotinylated p-MET antibody, and then washed in CyFACS buffer. The cocktail of the remaining metal-conjugated phospho-antibodies, including an anti-biotin secondary antibody, was added in 180 μL and incubated for 30 minutes at room temperature. After washing, cells were resuspended in 1 mL iridium-containing DNA intercalator (1:5,000 dilution in 1.6% PFA containing PBS) and incubated at 4°C. Cells were washed twice with MilliQ water, diluted to 750×10^5 cells/mL with 10% EQ Calibration Beads (Fluidigm), and acquired on CyTOF (Fluidigm).

Sample barcodes were resolved using a single-cell debarcoder tool (54). Individual samples were gated using Cytobank based on the iridium intercalator for intact cells, and then on singlets to exclude normalization beads, cellular debris, dead cells, and doublets for

the identification of CD34⁺, CD3⁺, and CD33⁺ cells for downstream analyses. The raw expression matrix of non-bead events was extracted using CellEngine and arcsinh-transformed (cofactor: 5), and the UMAP was generated using 21 cell-surface markers in R using uwot package. The cluster of cells that did not have signal for any marker were debris and excluded from further analyses, and the UMAP was regenerated. For cell-type assignment, the cells were first grouped into 200 clusters using clara clustering and mapped to the gated landmark populations based on the highest Pearson correlation of averaged expression profiles. The gated landmark populations were defined using CellEngine: After removing the normalization beads, the remaining events were gated into B (CD19⁺), HLA-DR⁺ (HLA-DR⁺CD123⁺), early blast (CD34⁺), NK (CD7⁺CD3⁺), T (CD8: CD3⁺CD8⁺CD4⁺; CD4: CD3⁺CD8⁻CD4⁺; double-positive: CD3⁺CD8⁺CD4⁺; double-negative: CD3⁺CD8⁻CD4⁻, CD24_{myeloid} (CD11c⁺CD24⁺), and late blast (CD33⁺CD11c⁺) cells. The median values for each sample per cell type were calculated using raw ion counts. CyTOF data were additionally analyzed as previously described using the SPADE tool (19).

scRNA-seq

PBMCs were collected from 11 patients on trial and 1 normal control at five distinct time points, except where indicated as missing (Supplementary Fig. S5A), for a total of 52 samples. These were evenly divided across five distinct scRNA-seq reactions using a Latin Square design so that each reaction contained equal numbers of pooled cells from distinct patients and days of collection to minimize batch effects. A normal control was included with each reaction to ensure uniformity across runs. In brief, frozen PBMCs were thawed at 37°C, resuspended in EasySep buffer (STEMCELL), and treated with DNaseI for 15 minutes at room temperature before filtering through a 40- μm filter. Cells were concentrated to 1,000 cells/ μL , pooled according to the matrix in Fig. 3A, and loaded in duplicate onto the 10x Chromium instrument (10x Genomics), with a target capture per well of 25,000 to 30,000 as per published protocol (23). The libraries were prepared using Chromium Single Cell 3' Reagent Kits v1 according to the manufacturer's protocol (10x Genomics) and sequenced using a custom program with asymmetrical pair-end read length as described previously on the Illumina HiSeq4000 (40). To determine the SNPs of the individual patients, extracted genomic DNA from PBMCs was genotyped using the Infinium OmniExpressExome-8 v1.6 BeadChip (Illumina).

scRNA-seq Data Analyses

CellRanger v1.2 was used to process the FASTQ files, align the sequencing reads to the hg19 transcriptome, and generate a filtered unique molecular identifier (UMI) expression profile for each cell. Pooled sample libraries were processed using freemuxlet, the genotype-free version of demuxlet, to predict clusters of cells from the same patient based on SNP concordance (23). Briefly, CellRanger-aligned reads were processed to generate a BAM file of reads overlapping a high-quality list of SNPs obtained from the 1000 Genomes Consortium (1KG; ref. 55). Freemuxlet was run on this filtered BAM file using the 1KG VCF file as a reference, the input number of samples per pool as a guideline for clustering groups of cells by SNP concordance, and all other default parameters. Barcodes were classified as either singlets, doublets, or ambiguous. Ambiguous and doublet events were excluded from further analysis. Freemuxlet-predicted clusters of cells were mapped to patients using BCftools gtcheck (parameters: -G 99) based on the similarity between the consensus SNP profile of freemuxlet clusters and the ground truth genotypes per patient identified via the Infinium OmniExpress-Exome-8 v1.6 BeadChip (Illumina; ref. 56). UMAP plots were generated with Monocle 3 (18, 26). Inspection of the top specific markers from cell partitions and automated cell assignments generated by

Seurat v4 were used to identify cell partitions. Gene modules were identified using the method of Cao and colleagues, and aggregated expression values in the early, late, and HLA-DR⁺ clusters were calculated according to sample class (normal control, responders, and progressive disease; ref. 32). GO term enrichment was determined using GOrilla (<http://cbl-gorilla.cs.technion.ac.il>) in target/background mode with all module genes serving as the background (33, 57). Redundant GO terms were filtered using REVIGO and summarized using semantic space plots (34). Sequencing data have been deposited at Gene Expression Omnibus (accession number: GSE162117). Mass cytometry data are available at <https://premium.cytoBank.org/cytoBank/experiments/149419>. Freemuxlet, Batchelor, and programming code may be accessed at <https://github.com/yelabucsf/popsicle>; <https://bioconductor.org/packages/release/bioc/html/batchelor.html>; and https://github.com/blaserlab/ficlatuzumab_aml.

Statistical Considerations

Survival was estimated using the Kaplan–Meier method, and survival comparisons were made by the Mantel–Cox log-rank test. The nonparametric Mann–Whitney test was used to compare the distributions of ratio in median of the expression at 24 and 48 hours post-ficlatuzumab normalized to baseline treatment between untreated versus treated patients and responders versus nonresponders. Because of the exploratory nature of this phase Ib investigation and the fact that each patient had multiple timed collections, these measurements were treated as distinct entities and pooled solely based on clinical response, irrespective of time or pervanadate stimulation. The Bonferroni correction was applied for multiple comparisons with an overall probability of significance defined as less than 0.05 using Prism 8.

Authors' Disclosures

G.K. Behbehani reports grants from The Ohio State University during the conduct of the study, as well as personal fees from Agios, other support from Fluidigm, and grants from Jazz Pharmaceuticals outside the submitted work. G.N. Mannis reports personal fees from AbbVie, Genentech, Agios, Bristol Myers Squibb/Celgene, Pfizer, Stemline, Astellas, Kite, and Novartis; personal fees and other support from Jazz and Forty Seven/Gilead; and other support from Glycomimetics outside the submitted work. R. Olin reports grants from Daiichi Sankyo, Pfizer, Cellectis; grants and personal fees from Genentech and Astellas; and personal fees from Jazz, Amgen, and AbbVie outside the submitted work. C.J. Ye reports personal fees from ImmunAI, Maze Therapeutics, TRex Bio, and Related Sciences outside the submitted work. D.P. Carbone reports personal fees from AstraZeneca, Daiichi Sankyo, Eisai, EMD Serono, Flame Biosciences, Gritstone, GlaxoSmithKline, Lilly, Sanofi, Seattle Genetics, Bristol Myers Squibb, Intellisphere, Janssen, Mirati, Novocure, Oncocyte, and Oncohost outside the submitted work. F. McCormick reports personal fees and other support from BridgeBio Pharma, Leidos Biomedical Research, Inc., Ideaya Biosciences, Pfizer, and Quartz, grants and personal fees from Daiichi, grants from Boehringer Ingelheim, other support from Olema Pharmaceuticals, and personal fees from Kura Oncology, PMV Pharma, PellePharm, and Quanta Therapeutics outside the submitted work; is a consultant for Amgen, Daiichi, Frontiers Med, Exuma Biotech, Ideaya Biosciences, Kura Oncology, Leidos Biomedical Research, Inc., PellePharm, Pfizer, PMV Pharma, and Quanta Therapeutics; is a consultant for and cofounder of the following companies (with ownership interest including stock options): BridgeBio Pharma, Olema Pharmaceuticals, and Quartz; is the scientific director of the National Cancer Institute (NCI) RAS Initiative at the Frederick National Laboratory for Cancer Research/Leidos Biomedical Research, Inc.; and has been a recipient of research grants from Daiichi and Gilead Sciences and has a current grant from Boehringer Ingelheim. C. Andreadis reports grants from Gateway

for Cancer Research and NCI R03 during the conduct of the study, as well as personal fees and nonfinancial support from Kite, grants, personal fees, and nonfinancial support from Novartis and Bristol Myers Squibb, grants from Merck, and personal fees from Astellas, Incyte, Karyopharm, Epizyme, TG Therapeutics, Atara Biotherapeutics, and Jazz Pharmaceuticals outside the submitted work. No disclosures were reported by the other authors.

Authors' Contributions

V.E. Wang: Conceptualization, resources, formal analysis, funding acquisition, investigation, visualization, methodology, writing—original draft, project administration, writing—review and editing. **B.W. Blaser:** Data curation, software, formal analysis, writing—review and editing. **R.K. Patel:** Data curation, software, formal analysis, visualization, methodology, writing—review and editing. **G.K. Behbehani:** Software, formal analysis. **A.A. Rao:** Software, formal analysis. **B. Durbin-Johnson:** Data curation, software. **T. Jiang:** Writing—review and editing. **A.C. Logan:** Resources, writing—original draft. **M. Settles:** Data curation, software, formal analysis. **G.N. Mannis:** Resources. **R. Olin:** Resources. **L.E. Damon:** Resources. **T.G. Martin:** Resources. **P.H. Sayre:** Resources. **K.M. Gaensler:** Resources. **E. McMahon:** Resources. **M. Flanders:** Resources. **V. Weinberg:** Formal analysis. **C.J. Ye:** Conceptualization, software, formal analysis, visualization, methodology. **D.P. Carbone:** Writing—review and editing. **P.N. Munster:** Resources. **G.K. Fragiadakis:** Data curation, formal analysis, writing—review and editing. **F. McCormick:** Supervision, writing—original draft. **C. Andreadis:** Conceptualization, resources, supervision, funding acquisition, writing—original draft, writing—review and editing.

Acknowledgments

This work is dedicated to the memory of our friend and colleague Georgia Hatzivassiliou. We thank Natalia Sigal and Holden Maecker for performing the CyTOF, Erin Simonds for technical advice regarding the CyTOF panel design and execution, Rene Bernards and Andrew Wolfe for discussion and critical reading of the manuscript, and the patients and their families for participating in the study. V.E. Wang was supported by K08 from the NCI (CA249744–01), the Damon Runyon Postdoctoral Award (121570), the ASCO Young Investigator Award (P0511381), a Lung Cancer Research Foundation Fellowship (LC170486), and the U.S. Department of Defense (W81XWH-17-1-0365 and W81XWH-18-1-0551). B.W. Blaser was supported by K08 from the National Institute of Diabetes and Digestive and Kidney Diseases (DK111920). C. Andreadis was supported by NCI R03 (5R03CA188236–02) and a Gateway for Cancer Research grant.

The publication costs of this article were defrayed in part by the payment of publication fees. Therefore, and solely to indicate this fact, this article is hereby marked “advertisement” in accordance with 18 USC section 1734.

Note

Supplementary data for this article are available at Blood Cancer Discovery Online (<https://bloodcancerdiscov.aacrjournals.org/>).

Received March 29, 2021; revised April 2, 2021; accepted June 14, 2021; published first July 16, 2021.

REFERENCES

- Gilliland DG, Tallman MS. Focus on acute leukemias. *Cancer Cell* 2002;1:417–20.
- Giles F, Vey N, DeAngelo D, Seiter K, Stock W, Stuart R, et al. Phase 3 randomized, placebo-controlled, double-blind study of high-dose continuous infusion cytarabine alone or with laromustine

- (VNP40101M) in patients with acute myeloid leukemia in first relapse. *Blood* 2009;114:4027–33.
3. Roboz GJ, Jabbour EJ, Faderl S, Douer D. Advances in the treatment of relapsed/refractory acute lymphoblastic leukemia: a case study compendium. *Clin Adv Hematol Oncol* 2014;12:8–18,1.
 4. Ravandi F, Ritchie EK, Sayar H, Lancet JE, Craig MD, Vey N, et al. Vosaroxin plus cytarabine versus placebo plus cytarabine in patients with first relapsed or refractory acute myeloid leukaemia (VALOR): a randomised, controlled, double-blind, multinational, phase 3 study. *Lancet Oncol* 2015;16:1025–36.
 5. Straussman R, Morikawa T, Shee K, Barzily-Rokni M, Qian ZR, Du J, et al. Tumour micro-environment elicits innate resistance to RAF inhibitors through HGF secretion. *Nature* 2012;487:500–4.
 6. Wilson TR, Fridlyand J, Yan Y, Penuel E, Burton L, Chan E, et al. Widespread potential for growth-factor-driven resistance to anticancer kinase inhibitors. *Nature* 2012;487:505–9.
 7. Kentsis A, Reed C, Rice KL, Sanda T, Rodig SJ, Tholouli E, et al. Auto-crine activation of the MET receptor tyrosine kinase in acute myeloid leukemia. *Nat Med* 2012;18:1118–22.
 8. Rosen EM, Nigam SK, Goldberg ID. Scatter factor and the c-met receptor: a paradigm for mesenchymal/epithelial interaction. *J Cell Biol* 1994;127:1783–7.
 9. Pons E, Uphoff CC, Drexler HG. Expression of hepatocyte growth factor and its receptor c-met in human leukemia-lymphoma cell lines. *Leuk Res* 1998;22:797–804.
 10. Hjorth-Hansen H, Seidel C, Lamvik J, Borset M, Sundan A, Waage A. Elevated serum concentrations of hepatocyte growth factor in acute myelocytic leukaemia. *Eur J Haematol* 1999;62:129–34.
 11. Kim JG, Sohn SK, Kim DH, Baek JH, Lee NY, Suh JS, et al. Clinical implications of angiogenic factors in patients with acute or chronic leukemia: hepatocyte growth factor levels have prognostic impact, especially in patients with acute myeloid leukemia. *Leuk Lymphoma* 2005;46:885–91.
 12. Verstovsek S, Kantarjian H, Estey E, Aguayo A, Giles FJ, Manshouri T, et al. Plasma hepatocyte growth factor is a prognostic factor in patients with acute myeloid leukemia but not in patients with myelodysplastic syndrome. *Leukemia* 2001;15:1165–70.
 13. Hino M, Inaba M, Goto H, Nishizawa Y, Tatsumi N, Nishino T, et al. Hepatocyte growth factor levels in bone marrow plasma of patients with leukaemia and its gene expression in leukaemic blast cells. *Br J Cancer* 1996;73:119–23.
 14. Bendall SC, Simonds EF, Qiu P, Amir el AD, Krutzik PO, Finck R, et al. Single-cell mass cytometry of differential immune and drug responses across a human hematopoietic continuum. *Science* 2011;332:687–96.
 15. Gubin MM, Esaulova E, Ward JP, Malkova ON, Runci D, Wong P, et al. High-dimensional analysis delineates myeloid and lymphoid compartment remodeling during successful immune-checkpoint cancer therapy. *Cell* 2018;175:1014–30.
 16. van Galen P, Hovestadt V, Wadsworth Ii MH, Hughes TK, Griffin GK, Battaglia S, et al. Single-cell RNA-seq reveals AML hierarchies relevant to disease progression and immunity. *Cell* 2019;176:1265–81.
 17. Dohner H, Estey E, Grimwade D, Amadori S, Appelbaum FR, Buchner T, et al. Diagnosis and management of AML in adults: 2017 ELN recommendations from an international expert panel. *Blood* 2017;129:424–47.
 18. Becht E, McInnes L, Healy J, Dutertre CA, Kwok IWH, Ng LG, et al. Dimensionality reduction for visualizing single-cell data using UMAP. *Nat Biotechnol* 2018 Dec 3 [Epub ahead of print].
 19. Behbehani GK, Samusik N, Bjornson ZB, Fantl WJ, Medeiros BC, Nolan GP. Mass cytometric functional profiling of acute myeloid leukemia defines cell-cycle and immunophenotypic properties that correlate with known responses to therapy. *Cancer Discov* 2015;5:988–1003.
 20. Levine JH, Simonds EF, Bendall SC, Davis KL, Amir el AD, Tadmor MD, et al. Data-driven phenotypic dissection of AML reveals progenitor-like cells that correlate with prognosis. *Cell* 2015;162:184–97.
 21. Corcoran RB, Rothenberg SM, Hata AN, Faber AC, Piris A, Nazarian RM, et al. TORC1 suppression predicts responsiveness to RAF and MEK inhibition in BRAF-mutant melanoma. *Sci Transl Med* 2013;5:196ra98.
 22. Blumenschein GR Jr, Mills GB, Gonzalez-Angulo AM. Targeting the hepatocyte growth factor-cMET axis in cancer therapy. *J Clin Oncol* 2012;30:3287–96.
 23. Kang HM, Subramaniam M, Targ S, Nguyen M, Maliskova L, McCarthy E, et al. Multiplexed droplet single-cell RNA-sequencing using natural genetic variation. *Nat Biotechnol* 2018;36:89–94.
 24. Pique-Regi R, Romero R, Tarca AL, Sandler ED, Xu Y, Garcia-Flores V, et al. Single cell transcriptional signatures of the human placenta in term and preterm parturition. *eLife* 2019;8:e52004.
 25. Park SR, Namkoong S, Friesen L, Cho CS, Zhang ZZ, Chen YC, et al. Single-cell transcriptome analysis of colon cancer cell response to 5-fluorouracil-induced DNA damage. *Cell Rep* 2020;32:108077.
 26. Trapnell C, Cacchiarelli D, Grimsby J, Pokharel P, Li S, Morse M, et al. The dynamics and regulators of cell fate decisions are revealed by pseudotemporal ordering of single cells. *Nat Biotechnol* 2014;32: 381–6.
 27. Haghverdi L, Lun ATL, Morgan MD, Marioni JC. Batch effects in single-cell RNA-sequencing data are corrected by matching mutual nearest neighbors. *Nat Biotechnol* 2018;36:421–7.
 28. Chung SS, Eng WS, Hu W, Khalaj M, Garrett-Bakelman FE, Tavakkoli M, et al. CD99 is a therapeutic target on disease stem cells in myeloid malignancies. *Sci Transl Med* 2017;9:eaaj2025.
 29. Hao Y, Hao S, Andersen-Nissen E, Mauck WM 3rd, Zheng S, Butler A, et al. Integrated analysis of multimodal single-cell data. *Cell* 2021;184:3573–87.e29.
 30. Edwards DK, Watanabe-Smith K, Rofelty A, Damernsawad A, Laderas T, Lambale A, et al. CSF1R inhibitors exhibit antitumor activity in acute myeloid leukemia by blocking paracrine signals from support cells. *Blood* 2019;133:588–99.
 31. Seiden-Long IM, Brown KR, Shih W, Wigle DA, Radulovich N, Jurisica I, et al. Transcriptional targets of hepatocyte growth factor signaling and Ki-ras oncogene activation in colorectal cancer. *Oncogene* 2006;25:91–102.
 32. Cao J, Spielmann M, Qiu X, Huang X, Ibrahim DM, Hill AJ, et al. The single-cell transcriptional landscape of mammalian organogenesis. *Nature* 2019;566:496–502.
 33. Eden E, Navon R, Steinfeld I, Lipson D, Yakhini Z. GOrilla: a tool for discovery and visualization of enriched GO terms in ranked gene lists. *BMC Bioinformatics* 2009;10:48.
 34. Supek F, Bosnjak M, Skunca N, Smuc T. REVIGO summarizes and visualizes long lists of gene ontology terms. *PLoS One* 2011;6:e21800.
 35. Peterson RT, Schreiber SL. Translation control: connecting mitogens and the ribosome. *Curr Biol* 1998;8:R248–50.
 36. Jefferies HB, Fumagalli S, Dennis PB, Reinhard C, Pearson RB, Thomas G. Rapamycin suppresses 5' TOP mRNA translation through inhibition of p70s6k. *EMBO J* 1997;16:3693–704.
 37. Reynaud D, Pietras E, Barry-Holson K, Mir A, Binnewies M, Jeanne M, et al. IL-6 controls leukemic multipotent progenitor cell fate and contributes to chronic myelogenous leukemia development. *Cancer Cell* 2011;20:661–73.
 38. Héroult A, Binnewies M, Leong S, Calero-Nieto FJ, Zhang SY, Kang YA, et al. Myeloid progenitor cluster formation drives emergency and leukaemic myelopoiesis. *Nature* 2017;544:53–8.
 39. Schürch CM, Riether C, Ochsnein AF. Cytotoxic CD8+ T cells stimulate hematopoietic progenitors by promoting cytokine release from bone marrow mesenchymal stromal cells. *Cell Stem Cell* 2014;14:460–72.
 40. Zheng GX, Terry JM, Belgrader P, Ryvkin P, Bent ZW, Wilson R, et al. Massively parallel digital transcriptional profiling of single cells. *Nat Commun* 2017;8:14049.
 41. Mair F, Erickson JR, Voillet V, Simoni Y, Bi T, Tzysnik AJ, et al. A targeted multi-omic analysis approach measures protein expression and low-abundance transcripts on the single-cell level. *Cell Rep* 2020; 31:107499.
 42. Trzupke D, Dunstan M, Cutler AJ, Lee M, Godfrey L, Jarvis L, et al. Discovery of CD80 and CD86 as recent activation markers on regulatory T cells by protein-RNA single-cell analysis. *Genome Med* 2020;12:55.
 43. Schwanhäusser B, Busse D, Li N, Dittmar G, Schuchhardt J, Wolf J, et al. Global quantification of mammalian gene expression control. *Nature* 2011;473:337–42.

44. Azimifar SB, Nagaraj N, Cox J, Mann M. Cell-type-resolved quantitative proteomics of murine liver. *Cell Metab* 2014;20:1076–87.
45. Stoeckius M, Hafemeister C, Stephenson W, Houck-Loomis B, Chattopadhyay PK, Swerdlow H, et al. Simultaneous epitope and transcriptome measurement in single cells. *Nat Methods* 2017;14:865–8.
46. Peterson VM, Zhang KX, Kumar N, Wong J, Li L, Wilson DC, et al. Multiplexed quantification of proteins and transcripts in single cells. *Nat Biotechnol* 2017;35:936–9.
47. Platanius LC. Mechanisms of type-I- and type-II-interferon-mediated signalling. *Nat Rev Immunol* 2005;5:375–86.
48. Zimmermann M, Arruda-Silva F, Bianchetto-Aguilera F, Finotti G, Calzetti F, Scapini P, et al. IFN α enhances the production of IL-6 by human neutrophils activated via TLR8. *Sci Rep* 2016;6:19674.
49. Blank CU, Rozeman EA, Fanchi LF, Sikorska K, van de Wiel B, Kvistborg P, et al. Neoadjuvant versus adjuvant ipilimumab plus nivolumab in macroscopic stage III melanoma. *Nat Med* 2018;24:1655–61.
50. Amaria RN, Reddy SM, Tawbi HA, Davies MA, Ross MI, Glitza IC, et al. Neoadjuvant immune checkpoint blockade in high-risk resectable melanoma. *Nat Med* 2018;24:1649–54.
51. Cheson BD, Bennett JM, Kopecky KJ, Buchner T, Willman CL, Estey EH, et al. Revised recommendations of the International Working Group for diagnosis, standardization of response criteria, treatment outcomes, and reporting standards for therapeutic trials in acute myeloid leukemia. *J Clin Oncol* 2003;21:4642–9.
52. National Cancer Institute. Common Terminology Criteria for Adverse Events (CTCAE). Version 4.0. Bethesda (MD): NCI; 2009. Publication No.: 03-5410. Available from: https://evs.nci.nih.gov/ftp1/CTCAE/CTCAE_4.03/CTCAE_4.03_2010-06-14_QuickReference_5x7.pdf.
53. Han G, Spitzer MH, Bendall SC, Fantl WJ, Nolan GP. Metal-isotope-tagged monoclonal antibodies for high-dimensional mass cytometry. *Nat Protoc* 2018;13:2121–48.
54. Zunder ER, Finck R, Behbehani GK, Amir el AD, Krishnaswamy S, Gonzalez VD, et al. Palladium-based mass tag cell barcoding with a doublet-filtering scheme and single-cell deconvolution algorithm. *Nat Protoc* 2015;10:316–33.
55. Auton A, Brooks LD, Durbin RM, Garrison EP, Kang HM, Korbel JO, et al. A global reference for human genetic variation. *Nature* 2015;526:68–74.
56. Li H. A statistical framework for SNP calling, mutation discovery, association mapping and population genetical parameter estimation from sequencing data. *Bioinformatics* 2011;27:2987–93.
57. Eden E, Lipson D, Yogev S, Yakhini Z. Discovering motifs in ranked lists of DNA sequences. *PLoS Comput Biol* 2007;3:e39.